Experimental determination of porosity and permeability changes induced by massive injection of CO_2 into carbonate reservoirs.

L. Luquot * and P. Gouze

Géosciences, Université de Montpellier 2, CNRS, Montpellier, France

**Corresponding author: Laboratoire Géosciences, Université Montpellier 2, CC MSE, 34095 Montpellier, France.*

Tel: 0033467149066

Fax: 0033467149088

Email: linda.luquot@msem.univ-montp2.fr

Abstract. Coupled transport-reaction numerical simulations are essential to model large-scale processes over long durations. However, in the case of CO_2 underground storage, few experimental data exist allowing us to constrain and validate the various assumptions implemented in these models. In particular, little is known about the (irreversible) modifications of reservoir properties in the highly reactive systems resulting from massive CO_2 injection. A set of four reactive flow-trough experiments at temperature T = 100 °C and total pressure P = 12 MPa are performed using limestone reservoir samples. The objectives are to quantify mass transfers occurring (1) near the injection well, where the aquifer fluid is almost saturated with CO_2 (i.e. $P_{CO_2} \approx P$), and (2) at increasing distances from the injection well, where the fluid is expected to display lower P_{CO_2} values and higher divalent cation concentrations resulting from rock dissolution along the fluid pathway.

The results for P_{CO_2} of 10 MPa and 6 MPa predict non-uniform dissolution features associated with transport-controlled mass transfer near the injection well, while kinetically-controlled uniform dissolution is observed at lower P_{CO_2} (2.5 MPa). Furthermore, the scaling laws relating porosity to permeability are distinctly different between experiments. As a result, macroscale porosity-permeability relationships should be parameterized not only to account for rock-type-dependent properties, as is generally the case when modelling low reactivity systems, but also to take account of the local dissolution regime. Therefore, we define a reference macroscopic Damköhler number (Da^* = 1) corresponding to the kinetically-controlled dissolution conditions observed at P_{CO_2} = 2.5 MPa. Then, the value of Da > 1 characterizing the transport-controlled dissolution is given by the ratio between the calcium production (normalized to the sample-size) obtained in experiments at P_{CO_2} > 2.5 MPa and at P_{CO_2} = 2.5 MPa. We propose a Damköhler-dependent relationship between porosity and permeability: $k \sim (\phi - \phi_c)^n$, where ϕ_c is the porosity at the percolation threshold and *n* a power law of *Da*. As *Da* is defined only from macroscopic measurable parameters (i.e. calcium concentration in the case of calcite dissolution), the proposed k-ϕ-Da law can be easily implemented in reservoir-scale numerical simulations. Finally, for the experiment at P_{CO_2} = 0.7, i.e. reproducing conditions far from the injection well, we observe a uniform decrease of the porosity associated with dolomitization of the reservoir. However, the rate of permeability decrease is not constant but grows strongly as the porosity approaches ϕ_c, indicating a probable clogging of the medium if dolomitization conditions persist.

Keywords: Geologic sequestration, carbon dioxide, hydrodynamic

1 Introduction

CO_2 sequestration in geological formations is increasingly being studied as a workable way of limiting the overload of CO_2 emissions in the atmosphere. CO_2 disposal into geological formations includes mainly deep-saline aquifers and depleted oil reservoirs, which represent storage capacities estimated around 10^{13} kg and 4 x 10^{11} kg, respectively (Holloway, 1997). The process consists in injecting supercritical more-or-less-pure CO_2 into the formation porosity through boreholes, following the same procedure routinely performed by the petroleum industry for enhancing oil recovery. Here, we focus on carbonate-rich rocks which are widely present in sedimentary reservoirs.

Whatever the rock composition, the progressive dissolution of CO_2 in the formation water (generally at thermodynamic equilibrium with the rock-forming minerals) leads to a decrease in its pH. As a result, there is a significant increase in the dissolution capacity of the CO_2-rich fluid and the main expected processes involve dissolution of carbonates and, eventually, the (alumino)silicates, depending on the kinetics of the individual reactions see reviews in Plummer et al. (1978) and Lasaga (1981). Near the injection well, where disequilibrium is maximal, dissolution processes are expected to affect (irreversibly) the mechanical and hydrodynamic properties of the host rock. Specifically, dissolution will lead to an increase in porosity and permeability as well as changes in the reactive surface. For a constant injection rate, the penetration distance of the dissolution front will be a complex function of all these time- and space-resolved modifications. Conversely, the increase of cation concentration produced by the carbonate dissolution will eventually produce supersaturated fluids with respect to carbonate minerals at the outermost front of the CO_2-rich plume. We would expect precipitation processes and then decreasing porosity and permeability.

Several experimental and theoretical studies have analysed the geochemical reactions between reservoir rocks and injected carbon dioxide. Most of these studies investigated the mass

transfers of calcite, dolomite and magnesite, in contact with acid solutions at low CO_2 partial pressures (i.e. $P_{CO2} < 0.1$ MPa and room temperature (Lund et al., 1975; Plummer et al., 1978; Chou et al., 1989; Compton and Unwin, 1990; Dreybrodt et al., 1996; Arvidson et al., 2003; Noiriel et al., 2005). Others studies have focused on measuring calcite and dolomite dissolution rates at $P_{CO2} > 0.1$ MPa and/or moderate temperature (≤ 80°C) (Alkattan et al., 1998; Gautelier et al., 1999; Pokrovsky et al., 1999b). Recently, Pokrovsky et al. (2005) measured the dissolution rates of calcite, dolomite and magnesite as a function of P_{CO2} (P_{CO2} ≤ 8 MPa), at moderate NaCl concentration (0.01 to 1.0 M) and pH ≤ 4. However, only few experimental studies have been published for P-T-P_{CO2} conditions corresponding to the anticipated *in situ* conditions during injection, i.e. T = 80-150 °C and P = 9 -20 MPa. For instance, Kaszuba et al. (2003, 2005) carried out dissolution/precipitation experiments at high temperature T = 200 °C and high pressure (P = 20 MPa) in a closed reactor using powdered rocks. These results are fundamental for understanding reaction paths and quantifying mass transfers in response to high P_{CO2} fluids. Nevertheless, to quantify the long-lasting presence of huge volumes of CO_2 in reservoirs, we need to address the essential issue of feedback effects due to mass transfer, which can modify the pore structure and the hydrodynamic properties of the reservoir. Fluid-rock mass transfers depend on several parameters (P_{CO2}, cation concentrations, flow rate or pressure head at the boundaries, reactive surface areas, porosity, permeability, tortuosity, etc). The behaviour of these coupled processes is unpredictable without the help of numerical modelling. However, a key difficulty remains the large variability of the characteristic scales and times of the hydrodynamic and chemical processes. Specifically, fluid flow and hydrodynamic transport are controlled by large-scale characteristics of the porous media (e.g. long-range correlation of the permeability field and boundary conditions), whereas chemical reactions are controlled by local parameters at the fluid mineral interfaces. Consequently, physics-based laws relating microscopic volume

changes to macroscopic changes in permeability are only available for very simple models of homogeneous porous media (i.e. stacked spheres). Otherwise, we need to make use of heuristic laws that simultaneously lump together and upscale all the processes relating mass transfer to hydrodynamic properties (Wong et al., 1984). At present, i.e. 70 years after the pioneering work of Kozeny (1927) and Carman (1937), most numerical models use power law permeability / porosity scaling for the reservoir to predict permeability changes triggered by fluid-rock mass transfers.

In carbonate-rich reservoirs, both the pore structure and the macro-scale distribution of the transport properties are complex as a result of many successive diagenetic events, whereas the chemical composition of the rock may be relatively simple. For highly reactive fluids such as high P_{CO2} fluids, coupled flow and dissolution processes may induce the formation of highly conductive and spatially correlated flow channels, often termed wormholes (Fredd, 1998). Wormholes grow because of the natural heterogeneity of the porous medium and the relatively fast dissolution of the carbonate phase under low pH conditions. Evidently, general laws relating permeability (k) to porosity (ϕ) cannot account for changes in the spatial correlation of properties such as observed in the presence of wormholes.

This study aims to provide experimental data that can be used to constrain the modelling of CO_2 injection and sequestration, and specifically the permeability / porosity scaling law. We present a set of reactive percolation experiments carried out at pressures (P) and temperatures (T) typical of *in situ* conditions. Experiments are designed to quantify reactions occurring near the CO_2 injection zone, where the aquifer fluid is saturated with CO_2. In addition, experiments were carried out at increasing distances from the injection point, where the fluid is expected to contain progressively less CO_2 and more divalent cations resulting from rock dissolution along the fluid pathway. The underlying idea is to obtain experimental control-points in space and time corresponding to the transport of CO_2 in the reservoir during the injection phase,

whereas a complete and continuous reproduction of these processes is clearly not feasible at the laboratory scale. The experimental protocol allows us to study the feedback between changes in porosity, permeability and rock structure induced by the mass transfer of rock-forming minerals due to reactive fluid percolation in the rock. The methodology combines chemical analysis of the fluid, continuous measurements of sample permeability and pore-scale characterization of the rock before and after each experiment using X-rays microtomography (XMT) 3D imaging.

Finally, the dataset are used to establish the dependence of the ϕ - k relationship on the CO_2 partial pressure and disequilibrium state of the fluid.

2 Materials and methods

2.1 Experimental approach

The experiments consisted of injecting CO_2-enriched fluid through a cylindrical sample core of 9 mm diameter (D) and 18 mm length (L). The four percolation experiments were carried out under *in situ* sequestration conditions (T = 100 °C and P = 12 MPa), using various partial pressures of CO_2 and different ion concentrations in rock-equilibrated fluids (brine) to simulate CO_2-saturated brine transport during the injection phase (Fig. 1). Table 1 presents the composition of the different fluids used in the four flow-through experiments. The geochemical code CHESS (van der Lee, 2002) was used to determine the pH of the injected CO_2-enriched fluids for different fixed P_{CO2} conditions and values of saturation index. The CO_2-enriched fluid was injected at constant flow rate, corresponding to $Q = 1.9 \times 10^{-8}$ $m^3.s^{-1}$ for the three first experiments and $Q = 1.0 \times 10^{-8}$ $m^3.s^{-1}$ for the fourth experiment. The first three experiments were performed at the same flow rate because we assumed these conditions

represent processes in the vicinity of the injection well, whereas experiment 4 was performed at lower flow rate to mimic flow rate far away from the injection well.

2.2 The percolation apparatus

A new experimental device (Fig. 2) was specifically engineered to reproduce *in situ* massive CO_2 injection in reservoir samples at the laboratory scale for temperatures ranging from 50 to 200 °C, reservoir static pressures of 7 to 20 MPa and a partial pressure of CO_2 increasing up to the static pressure. Resident fluids are generally moderate to high salinity brines, almost or completely equilibrated with the rock-forming minerals prio to the CO_2 injection. The experimental apparatus described below allows us to study systematically the processes for any combination of these parameters.

The five main specific components of the device are described below: 1) a motorized dual-piston pump system that produces the flow of reservoir brine, 2) a motorized piston pump containing liquid-phase CO_2 cooled at 5°C, 3) the CO_2-brine mixing system, 4) the percolation cell holding the sample, and 5) the back-pressure controller / sampling system (Fig. 2).

The two motorized piston pumps are equipped with displacement encoders, which allow an accurate control of the flow rate. This motorized dual pump system is operated to obtain a continuous brine flow rate ranging from 2.10^{-9} to $2.5.10^{-8}$ $m^3.s^{-1}$. The piston pump motion and the pneumatically-controlled valves are operated by a LabView-based software.

It is difficult to control the volume ratio of a two-phase fluid mixture (i.e. liquid brine and supercritical CO_2). To avoid this obstacle, the mixing of the brine with CO_2 is carried out at high pressure (6 to 20 MPa) but low temperature (i.e. 5 °C). Under these conditions, CO_2 is in

the liquid state, which allows us to set the brine/CO_2 volume ratio corresponding to the desired CO_2 saturation of the fluid, while at the same time controlling the mixture flow rate (Fig. 3). To summarize, CO_2 and brine are first mixed in a cooled coil (e.g. maintained at 5 °C) and then heated up to the target temperature in an oven-coated coil.

In the percolation cell, both axial and radial confining pressures are applied to the sample. To mimic natural confinement conditions, it is essential to apply a controlled confining pressure and balance the fluid injection to avoid deviatoric stresses that may damage the sample irreversibly. The axial confining pressure is applied by the axial piston, whereas the radial confining pressure is obtained by pressurization of the silicon jacket covering the sample. In our experiments, axial and radial pressures are maintained equal, at 112 % of the inlet pressure whatever its value. Therefore, we can avoid damaging the rock throughout the duration of the experiment. This system is essential to minimize stresses on the sample during pressure and temperature loading and unloading at the beginning and the end of the experiment, respectively. To achieve this objective, we make use of a pressure multiplier with a free-moving piston of dissymmetric diameter.

The minimal pressure required to avoid degassing of the CO_2 in the circuit is controlled by a back-pressure system that imposes a constant pressure drop whatever the flow rate. This control may become critical at low flow rates. Under such conditions, manual control is required using a micrometric valve to reduce the fluctuations to less than about 3%. These fluctuations have no impact on the permeability measurements because flow rate is in a steady state, storage is low and the pressure drop is measured continuously by a high-resolution differential pressure transducer.

The available flow rate ($2.10^{-9} \leq Q \leq 2.5.10^{-8}$ $m^3.s^{-1}$) enables the exploration of a wide range of hydrodynamic conditions. Specifically, this equipment allows us to explore the entire range of fluid-rock interactions (dissolution and/or precipitation) from fully kinetically-controlled to fully transport-controlled mass transfer processes.

2.3 Sample characterization

The samples studied here are oolitic limestones from the Mondeville formation of Middle Jurassic age (Paris Basin). The rock is essentially composed of recrystallized ooliths with a mean diameter of less than a few hundred of μm, partially cemented with micritic calcite. All the samples were analysed and compared by XMT, XRD (X-Ray Diffraction), SEM (Scanning Electron Microscope) and cathodoluminescence techniques, to check that samples cored alongside each other are chemically and physically similar. Sample volumes contain thousands of pores and can be regarded as a representative elementary volume (REV) of rock (de Marsily, 1981). While heterogeneities larger than the sample size are clearly not included in this REV, the experimental results can be easily upscaled to the reservoir scale in terms of matrix properties. Cathodoluminescence and SEM analyses of the four samples show no measurable differences of chemical or structural composition. Additional analyses on whole rocks give the similar composition of the four studied samples, which corresponds to a magnesium-calcite of formula $Ca_{\alpha}Mg_{\beta}CO_3$ with $\alpha = 0.99$ and $\beta = 0.01$. The initial porosity of samples calculated from post-processing the XMT images (Noiriel et al., 2005) are similar in the case of 3 samples ($\phi = 7.5 \pm 0.2$) and slightly lower ($\phi = 6.8$) in the case of 1 sample.

2.4 Monitoring changes in porosity and permeability

Sample-scale changes in permeability $k(t)$ are measured by measuring the pressure drop ΔP between the inlet and the outlet of the sample. According to Darcy's law, the ratio of the

volumetric flow rate Q [$m^3.s^{-1}$] to the pressure difference ΔP (Pa) scales linearly with the sample permeability k [m^2]:

$$k = -\frac{\mu L Q}{S \Delta P}, \quad (1)$$

where L is the length of the sample in the flow direction [m], S is the cross-sectional area of the sample [m²] and μ is the dynamic viscosity of the fluid [Pa.s].

The fluid is collected repeatedly from the outlet port, and then analysed for Ca^{2+} and Mg^{2+} concentrations using an inductively coupled plasma-atomic emission spectrophotometer (ICP-AES). The volume of dissolved calcite (V_{CaCO3}(t)) is as follows:

$$V_{CaCO_3}(t) = Q\, \upsilon_{CaCO_3} \int_{\tau=0}^{t} \alpha \Delta C_{Ca}(\tau) + \beta \Delta C_{Mg}(\tau) d\tau, \quad (2)$$

where υ_{CaCO_3} is the calcite molar volume (3.7×10^{-5} $m^3.mol^{-1}$), ΔC_{Ca} and ΔC_{Mg} are the difference of calcium and magnesium concentration respectively between the outlet and the inlet fluids and α and β are the fraction of Ca and Mg respectively in the calcite (α = 99 and β = 1). The sample-scale porosity $\phi(t)$ is given by:

$$\frac{\partial \phi(t)}{\partial t} = \frac{1}{V} \frac{\partial V_{CaCO_3}(t)}{\partial t}, \quad (3)$$

where V is the total sample volume (i.e. $V = \pi L D^2 / 4$). To integrate equation (3), we need to know the porosity at a given time t using, for instance, the XMT images. The procedure is presented below in section 3.2.

2.5 X-Ray Computed Micro-Tomography (XMT)

Before and after each experiment, rock samples were scanned by X-ray Computed Micro-Tomography (XMT) to characterize the pore-space geometry. The XMT technique is an unmatched tool for producing nondestructive three-dimensional images of rocks without any prior preparation (Flannery et al., 1987). In the present study, data acquisition was performed at the European Synchrotron Radiation Facility (ESRF) in Grenoble (France) using the ID19 beam-line. The principle of XMT is based on the 3D computed reconstruction of an object partially absorbent to X-rays, using a set of 2D detector readings acquired at different angular positions. A total of 1 500 x-ray readings were recorded, using an exposure time of 2 s at each angle and a rotational interval of 0.12 degree along the core axis (Fig. 4).

For each X-ray reading, the monochromatic X-ray beam passes through the sample and then reaches the scintillator, which converts it into visible light recorded by a high-speed digital CCD camera (2048 × 2048 pixels). The pixel resolution is 5.06 µm, which is a function of the optical bench setup. Synchrotron radiation provides several advantages over conventional X-ray sources, including the production of a homogeneous, parallel, monochromatic and highly coherent photon flux. This results in high-quality images having a resolution of about the size of the voxel dimension. For a given energy of incident X-ray beam (here 40 keV), the attenuation depends on the chemical composition of the rock, specifically, the atomic number of its components and their mass fraction per volume (i.e. the density). In mono-crystalline rocks such as the samples studied here, XMT images yield the distribution of densities in the rock, or in other words, 3D porosity maps.

3. Experimental results and discussion

Changes of permeability and porosity in porous media are attributed to dissolution and precipitation. These dynamic processes are constrained from concurrent measurements of evolving permeability, mineral mass flux and sample pore structure. Because of the non-

destructive nature of XMT imaging, we can also observe the progression of the chemical reaction over the porous sample as well as related morphological changes.

3.1. Mass transfers during reaction

Fig. 5 reports the normalized time-resolved Ca and Mg concentration $\Delta C_i(t) = C_i(t)\big|_{out} - C_i(t)\big|_{in}$ with *i* = Ca and Mg, for the four experiments denoted D1, D2, D3 and P1. By convention, we define *t* = 0 when the CO_2 pump is activated. Experiments D1, D2, D3 and P1 are set up to mimic mass transfers at the locations 1, 2, 3 and 4 shown in Fig. 1 respectively.

Dissolution experiments D1 - D3

The ratio $\Delta C_{Ca}(t)$ to $\Delta C_{Mg}(t)$ is roughly 99, which corresponds to the Ca/Mg mole fraction ratio of the whole rock, i.e. a magnesium-calcite of formula $Ca_{0.99}Mg_{0.01}CO_3$. $\Delta C_{Ca}(t)$ and $\Delta C_{Mg}(t)$ display similar trends indicating congruent dissolution of the rock (Fig. 5). From this point, we describe processes using $\Delta C_{Ca}(t)$ data alone, but in the calculations, such as for porosity (equations 2 and 3), we account for the Ca/Mg stoichiometry of the rock-forming calcite. For D1, D2 and D3, the initial increase of ΔC_{Ca} (for $t < \tau_0$ with $\tau_0 \leq$ 20 minutes) reflects the dispersion of the CO_2 front in the circuit and transient processes in the sample. Indeed, for $t < \tau_0$, $\partial_t C_{\mathrm{Ca}}\big|_{out} > 0$ (with $\partial_t(.)$ denoting the time derivative).

For $t \geq \tau_0$, ΔC_{Ca} decreases and tends to an asymptotic value at $t = \tau_e$, for example when $\tau_e \approx$ 90 minutes as in the case of D2. The period of decreasing ΔC_{Ca}, for $\tau_0 < t < \tau_e$, corresponds to preferential dissolution of the cement and oolith roughness microstuctures starting at the inlet and progressing to the outlet (Fig. 6). Then, when the cement is dissolved, the calcium flux at the outlet is linked to dissolution of the oolitic fraction, which appears to be almost stationary. The distinctly different dissolution regimes for D1, D2, and D3 are

characterized by the value of $\partial_t(\Delta C_{Ca})$ for $t < \tau_e$, the asymptotic value of $C_{\mathrm{Ca}}\big|_{out}$ for $t \geq \tau_e$ and the value of τ_e (Fig.5). The attainment of an asymptotic value corresponds to the occurrence of sample-averaged steady-state mass transfer.

Experiments D1, D2 and D3 display dissolution processes, i.e. $\Delta C_{Ca}(t) > 0$. Assuming that the Mg content of the rock is negligible, the dissolution reaction is predominantly

$$CaCO_3 + H^+ \rightarrow Ca^{++} + HCO_3^- \qquad (4)$$

with the equilibrium constant $K(T = 100°C) = a_{\mathrm{Ca}} a_{\mathrm{HCO3}} / a_{\mathrm{H}} = 0.168$, where $a_i = \gamma_i C_i$ denotes the activity of species i with activity coefficient γ_i evaluated using the modified Debye-Huckel formulation for ionic strengths up to at least 2 mol.L^{-1} (Bethke, 1996). The outlet concentrations $C_{\mathrm{Ca}}(t)\big|_{out}$ and $C_{Mg}(t)\big|_{out}$ are always lower than the equilibrium concentrations $\tilde{C}_{\mathrm{Ca}}$ and $\tilde{C}_{\mathrm{Mg}}$, respectively, highlighting the kinetic control of the dissolution reaction. Using the transition state theory (Lasaga, 1998), the instantaneous sample-scale effective reaction rate [mol.m^{-3}.s^{-1}] for calcite dissolution (equation 4) can be written as:

$$R_{eff} = \frac{r\, S_r \left(1 - \langle I \rangle\right)}{\phi\, V}, \qquad (5)$$

where the kinetics coefficient r is an intrinsic property of the reaction for a given pH profile (Lasaga, 1998) [mol.m^{-2}.s^{-1}], S_r is the reaction surface area of the sample and $\langle I \rangle$ is the sample-averaged saturation index. For $t \geq \tau_e$, this index is approximated by $\langle I \rangle = [I_{out} + I_{in}]/2$. The saturation index for calcite in the outlet fluid is given by

$$I_{out} = \frac{IAP}{K_{eq}} = \frac{a_{Ca^{2+}}\big|_{out}\ a_{HCO_3^-}\big|_{out}}{a_{H^+}\big|_{out}\ K_{eq}}, \qquad (6)$$

where IAP stands for the Ion Activity Product of the outlet fluid at time $t \geq \tau_e$. The value of I_{out} is 0.22 for D1, 0.28 for D2 and 0.60 for D3, whereas the saturation index for the inlet fluid, calculated by replacing the outlet fluid concentration by the inlet fluid concentration in equation (6), is 1.9×10^{-4} for D1, 5.3×10^{-4} for D2 and 22.9×10^{-4} for D3.

The experiments presented here clearly show the role of CO_2 partial pressure in driving the dissolution process. As described by Golfier et al. (2002), the dissolution mechanism, at the pore-scale, can be separated into three steps: i) transport (by diffusion and advection) of the reactants to the reaction surface, ii) heterogeneous reaction at the surface (i.e. surface reaction), and iii) transport of reaction products away from the surface. The effective kinetics is controlled by the slowest of these three steps. It is generally accepted that transport of the solute to and from the reactive surface is associated with similar characteristic times. Thus, we can consider two limit cases. If the characteristic time of reaction is short compared to the characteristic time of transport, the reaction is called transport-limited. Conversely, if the hydrodynamic renewal of the reactive fluid is high, then the reaction is reaction-rate-limited. This behaviour is characterized macroscopically by the sample-scale Damköhler number,

$$Da \equiv \frac{\langle \bar{\gamma} \rangle \, l}{\langle \bar{u} \rangle}, \quad \text{for } Pe >> 1, \tag{7}$$

where $\langle \bar{\gamma} \rangle$ is the sample-averaged reaction rate [s^{-1}], l is the pore length [m], $\langle \bar{u} \rangle$ is the sample-averaged seepage velocity magnitude [$m.s^{-1}$] and $Pe \equiv \langle \bar{u} \rangle \, l / d_0$ is the local Peclet number that characterise reactant renewing at the fluid-rock interface, with d_0 the molecular diffusion (7.5×10^{-10} $m^2.s^{-1}$ for Ca). Values of Pe are larger than 10^2 for experiments D1 to D3, so that the Pe condition for equation (7) is satisfied.

If $Da < 1$, dissolution is reaction-rate-limited, whereas dissolution is transport-limited if $Da > 1$. At the Darcy scale, with $Pe >> 1$, transport-limited dissolution will lead to non-

uniform dissolution. The localization of dissolution features is a result of positive feedback between the local increase of pore diameter and the renewal capacity of the fluid in these enlarged pores (Hoefner and Fogler, 1988; Golfier et al., 2002). In this case, we would expect the formation of highly conductive flow channels, known as wormholes. The distribution and shape of the wormholes are controlled by the (initial) heterogeneity of the pore structure and the correlation length of the (initial) permeability field. For the value of Pe encountered here, we expect the properties of the wormholes to be independent of Pe because the diffusive transport is negligible.

Using equation (5), the sample-averaged reaction rate $\langle \bar{\gamma} \rangle$ is

$$\langle \bar{\gamma} \rangle = \frac{r\, S_r\, (1-\langle I \rangle)}{\langle \phi \rangle\, V\, (\Delta C_{Ca})^*}, \tag{8}$$

where $(\Delta C_{Ca})^*$ is the asymptotical, *i.e.* for $t >> \tau_e$, calcium mass balance in the sample (i.e. $C_{\mathrm{Ca}}\big|_{out} - C_{\mathrm{Ca}}\big|_{in}$) for $Da = 1$. Note that $\langle I \rangle$, $\langle \phi \rangle$ and S_r are time dependent. Conversely, the instantaneous Ca asymptotical mass balance in the sample, for $Da \neq 1$, is

$$C_{\mathrm{Ca}}\big|_{out} \approx C_{\mathrm{Ca}}\big|_{in} + \frac{r\, S_r\, (1-\langle I \rangle)}{Q}. \tag{9}$$

Note that the Ca concentration at the outlet is independent on the initial porosity. Combining equations (7) to (9), we obtain the expression of the Damköhler number as a function of the Ca concentration balance alone:

$$Da = \left(\Delta C_{Ca}\right) \Big/ (\Delta C_{Ca})^*. \tag{10}$$

By definition, $Da < 1$ denotes a reaction-rate-limited behaviour that we assume reflects homogeneous dissolution in the sample. While such is the case for D3 (Fig. 7 and 8), we observe significant wormhole structures for D2. Consequently, the value of $(\Delta C_{Ca})^*$ is evidently close to the value of $C_{\mathrm{Ca}}\big|_{out} - C_{\mathrm{Ca}}\big|_{in}$ measured for D3. In the following, we assume

that $(\Delta C_{Ca})^*$ is equal to $C_{\mathrm{Ca}}\big|_{out} - C_{\mathrm{Ca}}\big|_{in}$ measured for D3 at $t \geq \tau_e$. Hence, Da = 7.5 for D1 and Da = 3.1 for D2, corresponding to transport-limited dissolution. The expected patterns of dissolution localization are confirmed by the XMT images obtained for experiments D1 and D2 (Fig. 7 and 8). Clearly, the properties of the wormholes are controlled by the composition of the fluid. For experiment D1, we observe the formation of several conical penetrative wormholes as described by Golfier et al. (2002). Experiment D2 displays a more diffuse pattern of wormholes.

Precipitation

For experiment P1, fluid analysis shows that $\Delta C_{Ca} \approx 0$ and $\Delta C_{Mg} < 0$ whatever the value of *t*. Precipitation is likely associated with either magnesite precipitation or dolomitization of the calcite. The value of $C_{\mathrm{Mg}}\big|_{out}$ decreases by 47% for $t < t_e$, with $t_e \approx$ 600 minutes, then stabilizes at around 0.98×10^{-3} mol.L^{-1} for $t \geq t_e$. SEM imaging coupled with chemical analysis yields a magnesium-calcite of formula $Ca_{\alpha}Mg_{\beta}CO_3$ with α = 0.88-0.96 and β = 0.04-0.12 localized at the oolith surfaces (Fig. 9). Consequently, the dominant process is dolomitization.

3.2. Porosity and permeability changes

As stated in section 2.4, we require a reference value of the porosity to calculate the porosity by integration of equation (3). Porosity measured by processing the XMT data (Noiriel et al., 2005) is expected to be misevaluated because of the cutoff scale imposed by the voxel size dimension. Indeed, the surface roughness and microstructures of the micritic cement are not properly resolved because they are on a smaller scale than the XMT resolution (i.e. 5.06 µm). Nevertheless, both the cements and oolith roughness microstructures display large reactive

surface-areas and are dissolved in the early stage of the experiments (i.e. $t < \tau_e$). For each of the dissolution experiments, the porosity measured by XMT at the end of the experiment is the best evaluation of the true porosity. Consequently, using equation (3), we can write the sample-averaged porosity for a given experiment as follows:

$$\phi(t) = \phi^* - \frac{\left(V_{CaCO_3}\right)^* - V_{CaCO_3}(t)}{V}, \quad (11)$$

where ϕ^* and $\left(V_{CaCO_3}\right)^*$ are the porosities obtained by XMT and the volume of dissolved calcite at the end of the experiment, respectively. In the case of experiment P1, the reference porosity is taken at $t = 0$. Equation (11) can then be rewritten as $\phi(t) = \phi^{(0)} + \left(V_{CaCO_3}(t) - \left(V_{CaCO_3}\right)^{(0)}\right)/V$ in this case. Consequently, we expect a higher uncertainty on the value of the initial porosity $\phi^{(0)}$. Fig. 10 presents the sample-averaged change in porosity for the four experiments (D1, D2, D3 and P1). For $\tau_0 < t < \tau_e$, the porosity trends, $\phi(t)$, display a pre-asymptotic decrease corresponding to dissolution of the smaller structures (e.g. cements) in experiments D1 to D3. This pre-asymptotic decrease reflects the migration of the dissolution front from the inlet to the outlet of the sample. Then, for $t \geq \tau_e$, the dissolution rate ($\partial_t \phi$) tends to a constant value, while dissolution of the oolith surface becomes homogeneous. Similar results were obtained by Gouze et al. (2003) for the dissolution of initially rough-walled fractures in carbonate, as well as by Noiriel et al. (2004) for the dissolution of a porous limestone sample at low temperature. This behaviour is more marked in experiments D1 and D2, where dissolution is initially concentrated in the vicinity of the inlet as shown in Fig. 7. The values of $\partial_t \phi$, $\forall t$, are higher for experiment D1 and lower for experiments D2 and D3, highlighting the higher reactivity of the fluids at higher P_{CO_2}.

In the precipitation experiment (P1), we observe a steady decrease in porosity during the 700 minutes run time. Precipitation features cannot be visualized by the XMT technique, because they are smaller than the XMT resolution (5.06 µm).

Fig. 11 shows the corresponding changes in permeability with time $k(t)$. We derive a measure of $k(t)$ from the differential pressure records using equation (1) with a constant flow rate. As expected, permeability increases in the three dissolution experiments (D1 - D3), whereas it decreases in the precipitation experiment (P1). We should point out that the samples used for the three dissolution experiments are similar, with an initial permeability of around 35×10^{-15} m^2, while the sample used in experiment P1 has a higher initial permeability (i.e. 180×10^{-15} m^2), even all samples were taken side-by-side from the same core.

Permeability changes are clearly linked to the P_{CO_2} value as well as the Ca concentration in the inlet fluid. Experiments D1 and D2 display well-marked dual slope permeability trends corresponding to the dissolution regime change at $t = \tau_e$. The rate of increase in permeability, $\partial_t k$, is almost stationary for experiment D3, which, conversely, displays uniform dissolution behaviour. For experiment P1, $k(t)$ is characterized by two distinctly different rates, which are nevertheless associated with a single rate of decrease in porosity (Fig. 10). The origin of this behaviour is discussed in the next section.

3.3. Determination of Da-controlled $\partial k / \partial \phi$ laws

The distinctly different porosity and permeability trends obtained in experiments D1 – D3 characterize dissolution patterns controlled by initial CO_2 partial pressure and calcite saturation index. We should bear in mind that the saturation index depends on Ca concentration alone, because all the other parameters are constant and the rock samples are identical. Up to this point in the discussion, our results show that dissolution can display

distinctly different patterns along the path followed by CO_2-enriched fluids in the reservoir. However, we cannot use this observation to model reservoir-scale processes until both the porosity changes and the related permeability changes are parameterized according to the fluid composition. Hence, our objective is to establish a relation between the measured sample-scale porosity-permeability relationship and the value of *Da*.

Permeability is an intrinsic macroscopic property of the rock that results from a combination of several parameters including the geometry of the pores and throats, as well as, more importantly, the sample-scale connectivity of the voids (Mavko and Nur, 1997; Pape et al. 1999). In spite of this complexity, the essential behaviour can often be evaluated successfully from the porosity ϕ using power-law relationships such as the Kozeny-Carman model (Kozeny, 1927; Carman, 1937): $k \equiv \lambda \phi^n / S^m$, where S is the specific surface-area, and λ is a geometric factor expressing all the other rock-specific static parameters, while n and m reflect the dynamic behaviour of the relation. For example, the values of n and m for homogeneous sandstones (e.g. Fontainebleau sandstones) are close to 3 and 2, respectively (Bernabé et al., 2003). Evidently, in the case of rocks displaying complex pore structures, such as low-porosity carbonate rocks, the specific surface-area is not measurable and is certainly not the main parameter controlling permeability. Several alternative relations have been proposed to account for deviations from the Kozeny-Carman model. In instance, Bourbié et al. (1987) proposed the scaling relation $k \equiv \lambda' \phi^n d^2$, where d is the grain diameter. However, it is not easy to measure the grain diameter in most limestone rocks because of the large granulometric variability and marked anisotropy of the "grain" shape. For low-porosity media, it is often observed that changes in permeability scale with porosity only if $k \sim \phi^n$ for a given rock type (Bernabé et al., 1982). The simplest relationship is

$$k \equiv \theta(\phi - \phi_c)^n, \tag{12}$$

where the unit scaling and constant parameters characterizing the rock and the mass transfer processes are lumped together in θ an n, respectively. In equation (12), ϕ_c is the value of porosity at the percolation threshold ($k = 0$ if $\phi = \phi_c$). A similar power-law relationship was used by Noiriel et al. (2004) to account for the course of limestone dissolution. These authors (*op.cit*.) show that this relation gives rise to an asymptotic trend under conditions of dominantly homogeneous dissolution. However, while also being considered as independent of porosity, the value of θ is valid for a specific range of porosity that must be defined experimentally.

Figure12 shows the evolution of permeability versus porosity during experiment P1. We note that P1 is characterized by dolomitization of the oolith surfaces, with both ϕ and k decreasing. The plot of log(ϕ) vs. log(k) reveals two trends with a transitional behaviour between $t = t_p$ = 400 min and $t = t_e$ = 600 min. In the first part of the experiment, for $t < t_p$, the log(ϕ) vs. log(k) plot is linear and equation (8) can be applied with a very low value of the power law exponent: n = 0.18. Conversely, for $t > t_e$, log(ϕ) vs. log(k) is not linear, i.e. $\partial(\log(k))/\partial(\log(\phi)) > 0$. This indicates that porosity approaches the percolation threshold ϕ_c. We use a polynomial approximation to evaluate $\phi_c \approx 0.059$.

Fig. 13 shows the variation of permeability as a function of porosity during the dissolution experiments D1 – D3. For experiment D1, the variation of log(ϕ) vs. log(k) displays a dual slope behaviour reflecting the dual dissolution regime illustrated by the porosity profile in Fig. 7. It is difficult to interpret the value of n = 0.79 obtained when $\tau_0 < t < \tau_e$ because this result reflects both the low increase in permeability in the outlet side of the sample and the high increase in porosity near the inlet. For this experiment, the useful part of the log(ϕ)

vs. log(k) plot is the segment characterizing the stationary dissolution process, i.e. $t > \tau_e$, i.e. when the value of $n_{(D1)}$ = 4.79.

For experiment D2 and D3, we obtain a single-slope log(ϕ) vs. log(k) plot for $t > \tau_0$ with $n_{(D2)}$ = 1.24 and $n_{(D3)}$ = 0.29, respectively. This result is somewhat surprising because it implies that the change in permeability with porosity can be described as a single phenomenological process, while the rate of calcium production $\partial_t C_{\mathrm{Ca}}\big|_{out}$ is not stationary for $\tau_0 < t < \tau_e$. Physically, this means that, when a high rate of dissolution is associated with high S_r for cements and oolith rough surfaces, the slope (i.e. $\partial k / \partial \phi$) obtained for $\tau_0 < t < \tau_e$ is identical to the slope for $t > \tau_e$, when the dissolution rate is slower because of the lower value of S_r. In other words, for a given volume of dissolved calcite, dissolving cements and oolith surface roughness is less efficient in terms of increasing the permeability than dissolving massive ooliths. This behaviour is probably linked to the hydro-chemical history of the specific rock studied here, which displays high permeability (35×10^{-15} m^2) and low porosity. Indeed, this sequence from the Middle Jurassic of the Paris Basin corresponds to an aquifer with considerable flow of fluids having a composition very close to equilibrium (Coudrain and Gouze, 1993). Thus, we can assume that the slow redistribution of mass over several million years has acted to minimize the hydraulic energy loss. Consequently, these slow processes lead to a redistribution of micritic phases into zones where fluid flow is slow (i.e. in pore voids), while strategic flowpaths such as pore throats remain free of micritic growths. These features can be seen from microscope observations of the rock thin-sections.

The $k - \phi$ relationships are clearly linked to fluid chemistry for $Pe >> 1$; under this condition, n increases with Da. Consequently, the parameterization of the $k - \phi$ power law is required for predictive reservoir (Darcy scale) modelling. In large-scale meshed-reservoir

simulators, the local averaged Da (equation 10) can be easily calculated from the local (nodal) values of reactant concentration in the fluid. Fig. 14 shows the relationship between n and Da, which appears to be scaled according to a power law: $n = A + B\,Da^{C}$, where $A + B$ gives the value of n for $Da = 1$, i.e. $n = 0.29$, and C is the scaling exponent. The best fit is

$$n = 0.10 + 0.18\,Da^{1.60} \qquad (13)$$

Note that the value of C is independent of the uncertainties associated with the definition of $\left(\Delta C_{Ca}\right)^{*}$ (see equation 10), while the value of B is controlled by the value of n for $Da = 1$. A better evaluation of B would require performing experiments with P_{CO_2} ranging between the conditions used for experiments D2 and D3. Conversely, the value of A is independent of the uncertainties associated with the definition of $\left(\Delta C_{Ca}\right)^{*}$, provided the value of n measured for experiment D3 is indeed the lower value associated with $Da = 1$. This can be checked by performing an experiment with P_{CO_2} lower than the value used for experiment D3.

4. Conclusion

We present a set of four flow-through experiments allowing us to describe mass transfer processes (1) in the vicinity of the injection well where P_{CO_2} is maximal and dissolution is non-uniform, and (2) at distant locations where dissolution becomes more and more uniform, up to a point where precipitation (calcite dolomitization) is observed. This set of experiments is performed for $P - T - P_{CO_2}$ conditions representative of the most probable *in situ* conditions.

As a general rule, we expect non-uniform dissolution to occur near the injection well in calcite-rich reservoirs because of the high reactivity of calcite at low pH conditions. The experiment performed with P_{CO_2} close to the total pressure P supports the formation of highly conductive long-distance correlated flow channels, indicating transport-controlled dissolution.

These features strongly modify the permeability, while the macroscopic porosity is only moderately affected. For intermediate values of P_{CO_2}, the mass transfer changes from transport-controlled to kinetically-controlled dissolution. Uniform dissolution is obtained for P_{CO_2} = 2.5 MPa. These three dissolution experiments display distinctly different scaling laws relating the variations of porosity against permeability. Clearly, classical laws relating permeability (*k)* to porosity (ϕ) using rock-dependent parameterization alone cannot account for changes in permeability triggered by local fluid-rock disequilibrium. Hence, macroscale porosity-permeability relationships must be parameterized not only to reflect the rock-type-dependent properties, as generally performed when modelling low-reactivity systems, but also to take account of the local dissolution regime.

Finally, for the experiment with P_{CO_2} = 0.7, i.e. reproducing conditions far from the injection well, we observe a uniform decrease of the porosity associated with dolomitization of the reservoir. However, the rate of decrease in permeability rises sharply as the porosity approaches ϕ_c, indicating a probable clogging of the medium if dolomitization conditions persist.

Using this set of experiments, we extract step by step the macroscopic parameters required to formulate the dependence of the porosity-permeability scaling on local fluid-rock disequilibrium:

1) The value of porosity at the percolation threshold is evaluated using the precipitation experiment (P_{CO_2} = 0.7),
2) The sample-scale threshold value of the Damkolher number (*Da* = 1) is defined from the uniform dissolution experiment (P_{CO_2} = 2.5),

3) The value of *Da* for each of the non-uniform dissolution experiments (i.e. with P_{CO_2} = 6.0 and 10 MPa) is calculated from the amount of calcium produced in the sample,
4) The exponent *n* of the porosity-permeability power law in the relation $k \sim (\phi - \phi_c)^n$ is measured from the asymptotic dissolution regime for each of the experiments,
5) The relationship *n* versus *Da* is fitted to produce a macroscopic phenomenological law that can be upscaled easily to be implemented in classical reservoir numerical simulators.

Interestingly, we find that the relation between *n* and *Da* is a power law similar to the porosity-permeability scaling relationship. Evidently, the coefficients of this law are (highly) dependent on the properties of the reservoir and must be measured case by case. The new experimental apparatus and procedure described here probably represent the best approach to measure these parameters.

It is beyond the scope of our study to calculate systematically the errors generated by adopting a porosity-permeability scaling law that is independent of the local chemical disequilibrium, even though such an approach is commonly used in modelling. However, in view of the large value (C = 1.6) of the exponent in the power law scaling relation $n \sim Da^C$, any errors produced by assuming a constant value of *n* would clearly jeopardize the assessment of risks associated with the injection and long-term underground storage of CO_2 in limestones.

Acknowledgements

This work was supported by TOTAL S.A. and ADEME (Agence De l'Environemment et de la Maîtrise de l'Energie). These sources of funding are gratefully acknowledged.

References

Alkattan, M., Oelkers, E. H., Dandurand, J. L., Schott, J., 1998. An experimental study of calcite and limestone dissolution rates as a function of pH from -1 to 3 and temperature from 25 to 80 °C. Chem. Geol. 151, 199- 214.

Arvidson, R.S., Evren Ertan, I., Amonette, J.E., Luttge, A., 2003. Variation in calcite dissolution rates: a fundamental problem? Geochim. Cosmochim. Acta, 67, 1623 - 1634.

Bernabé, Y., Brace, W.F., Evans, B., 1982. Permeability, porosity and pore geometry of hot-pressed calcite. Mech. Mater. 1, 173–183.

Bernabé, Y., Mok, U., Evans, B., 2003. Permeability-porosity Relationships in Rocks Subjected to Various Evolution Processes. Pure and Applied Geophysics 160 (5-6), 937-960.

Bourbié, T., Coussy, O., Zinszner, B., 1987. Acoustics of porous média, Editions Technip, Paris.

Carman, P. C., 1937. Fluid flow through granular beds, Transaction for Institute of Chemical Engineer 15, 150-166.

Chou, L., Garrels, R. M., Wollast, R., 1989. Comparative study of the kinetics and mechanisms of dissolution of carbonate minerals, Chemical Geology, 78, 269-282.

Compton, R.G., and Unwin P. R., 1990. The dissolution of calcite in aqueous solution at pH<4: kinetics and mechanism. Philos. Trans. R. Soc. Lond. Ser. A: Math. Phys. Sci. 330, 1 - 45.

Coudrain-Ribstein A. and Gouze Ph., 1993. Quantitative Study of Geochemical Processes in the Dogger Aquifer (Paris Basin, France). Applied Geochemistry 8, 495-506.

Dreybrodt, W., Lauckner, J., Zaihua, H., Svensson, U., Buhmann, D., 1996. The kinetics of the reaction CO2+H2O=H++HCO3_ as one of the rate limiting steps for the dissolution of calcite in the system H2O–CO2–CaCO3. Geochim. Cosmochim. Acta.60, 3375–3381.

Flannery, B., Deckman, H., Roberge, W., D'Amico, K., 1987. Three-dimensional X-ray microtomography, Science 237, 1439 - 1443.

Fredd, C.N., and Fogler H. S.,1998. Influence of transport and reaction on wormhole formation in porous media. AIChE J. 44 (9), 1933 – 1949.

Gautelier, M., Oelkers, E. H., Schott, J., 1999. An experimental study of dolomite dissolution rates as a function of pH from -0.5 to 5 and temperatures from 25 to 80 °C. Chem. Geol. 157, 13 - 26.

Golfier, F., Zarcone, C., Bazin, B., Lenormand, R., Lasseux, D., Quintard, M., 2002. On the ability of a Darcy-scale model to capture wormhole formation during the dissolution of a porous medium. J. Fluid Mech. 457, 213 - 254.

Gouze, P., Noiriel, C., Bruderer, C., Loggia, D., Leprovost, R., 2003. X-Ray tomography characterisation of fracture surfaces during dissolution, Geophysical Research Letters 30, 1267, doi:1210.1029/2002/GL016755.

Hoefner, M.L., and Fogler, H. S., 1988. Pore Evolution and Channel Formation During Flow and Reaction in Porous Media, AIChE J. 34 (1), 45-54.

Holloway, S., 1997. An overview of the underground disposal of carbon dioxide. Energy Convers. Manag. 38, 193 - 198.

Kaszuba, J.P., Janecky, D. R., Snow, M. G., 2003. Carbon dioxide reaction processes in a model brine aquifer at 200°C and 200bars: implications for geologic sequestration of carbon. Appl. Geochem. 18 (7), 1065 - 1080.

Kaszuba, J.P., Janecky, D. R., Snow, M. G., 2005. Experimental evaluation of mixed fluid reactions between supercritical carbon dioxide and NaCl brine: Relevance to the integrity of a geologic carbon repository, Chem. Geol. 217 (3-4), 277 - 293.

Kozeny, J., 1927. Uber kapillare Leitung des Wassers im Boden. Sitz. Akad. Wissensh. 136, 271-306.

Lasaga, A. C., 1998. Kinetic theory in the earth sciences, Princeton University Press, (in New Jersey).

Lasaga, A. C., and Kirkpatrick, R. J., 1981. Kinetics of geochemical processes. Reviews in Mineralogy vol. 8, Mineralogical society of America ed., 398 pp.

van der Lee, J., De Windt, L., Lagneau, V., Goblet, P., 2002. Presentation and application of the reactive transport code HYTEC, Developments in Water Science 47, 599-606.

Lund, K., Fogler, H. S., McCune, C. C., 1975. Acidization: II. The dissolution of calcite in hydrochloric acid. Chem. Eng. Sci. 30, 865.

Mavko, G., and Nur, A., 1997. The effect of a percolation threshold in the Kozeny-Carman relation. Geophysics 62 (5), 1480-1482.

de Marsily, G., 1981. Hydrogéologie quantitative. (Ed.) Masson, Paris.

Noiriel, C., Gouze, Ph., Bernard, D., 2004. Investigation of porosity and permeability effects from microstructure changes during limestone dissolution, Geophysical Research Letters 31, L24603, doi:10.1029/2004GL021572.

Noiriel, C., Bernard, D., Gouze, Ph., Thibaut, X., 2005. Hydraulic properties and microgeometry evolution in the course of limestone dissolution by CO2-enriched water. Oil and Gas Science and Technology 60 (1), 177-192.

Pape, H., Clauser, C., Iffland, J., 1999. Permeability prediction based on fractal pore-space geometry. Geophysics 64 (5), 1447-1460.

Plummer, L. N., Wigley, T.M.L., Parkhurst, D.L., 1978. The kinetics of calcite dissolution in CO2-water systems at 5° to 60°C and 0.0 to 1.0 atm CO2. American Journal of Science 278, 179-216.

Pokrovsky, O.S., Schott, J., Thomas, F., 1999b. Dolomite surface speciation and reactivity in aquatic systems. Geochim. Cosmochim. Acta 63, 3133 - 3143.

Pokrovsky, O.S., Golubev, S. V., Schott, J., 2005. Dissolution kinetics of calcite, dolomite and magnesite at 25 8C and 0 to 50 atm pCO2, Chem. Geo., 217 (3-4), 239 – 255.

Wong, P.Z., Koplik, J., Tomanic, J. P., 1984. Conductivity and permeability of rocks, Physical Review B 30, 6606 - 6614.

Figure captions

Fig. 1: Schematic illustration of a CO_2 storage facility in a sedimentary reservoir. Boxes 1 to 4 represent the decrease of CO_2 partial pressure along fluid transfer pathways into a host reservoir. For our experiments, in box 1: P_{CO_2} = 100 bar (D1), box 2: P_{CO_2} = 60 bar (D2), box 3: P_{CO_2} = 25 bar (D3) and box 4: P_{CO_2} = 7 bar (P1).

Fig. 2: Diagram of the experimental setup.

Fig. 3: P - T phase diagram for CO_2, with P-T path corresponding to CO_2-brine mixing.

Fig. 4: Sketch diagram of the X-ray microtomography acquisition line.

Fig. 5: Normalized time-resolved concentrations of *Ca* (on right) and *Mg* (on left). Results are presented for each experiment, D1 (circles), D2 (squares), D3 (diamonds) and P1 (crosses). Note that the time scale for the dissolution experiment is not the same as for the precipitation experiment.

Fig. 6: XMT cross-section of the sample used for experiment D1. Left column shows the X-ray images before and after the dissolution experiment. Grey levels indicate the X-ray absorption intensity. Middle column shows the corresponding binary images, with calcite indicated in white and voids in black. Dissolved calcite (in white) is visualized on the right hand figure.

Fig. 7: *x-y* averaged porosity profiles along the samples in the flow direction (*z*) before the experiment (dotted) and after the experiment (plain).

Fig. 8: 3D XMT images of the cores before (top line) and after (bottom line) for experiments D1, D2 and D3. Black and white areas represent voids and solids, respectively. Image dimensions are: diameter 9 mm and height 4.5 mm.

Fig. 9: Secondary electron micrographs (SEM) showing dolomite precipitated during experiment P1.

Fig. 10: Variation of porosity with elapsed time; D1 (circles), D2 (squares), D3 (diamonds) and P1 (crosses).

Fig. 11: Variation of sample permeability with elapsed time for the dissolution experiments (D1 – D3) and the precipitation experiment P1.

Fig. 12: Log permeability versus log porosity for the precipitation experiments.

Fig. 13: Log permeability versus log porosity for the dissolution experiments D1 (circles), D2 (squares) and D3 (diamonds).

Fig. 14: Scaling exponent *n* versus value of the Damkolher number *Da* for the dissolution experiments D1 – D3. The regression coefficient *R* is optimal (R^2 = 1).

Species ($mg.L^{-1}$)	D1	D2	D3	P1
Na	23 000	23 000	23 000	23 000
Ca	330	375	400	3500
Mg	4	4.5	5	45
Cl	35 000	35 000	35 000	35 000
CO_2 ($mol.L^{-1}$)	0.8	0.5	0.2	0.06
pH	3.21	3.51	4.02	8.7

Table 1: Composition of fluids for experiments D1, D2, D3 and P1 (in $mg.L^{-1}$).

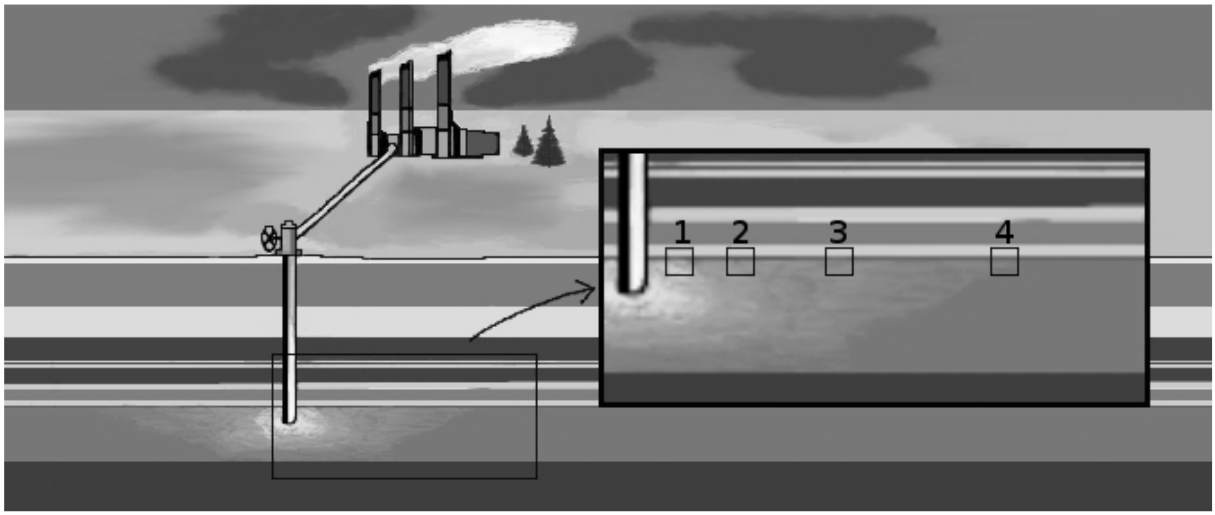

Fig. 1: Schematic illustration of a CO_2 storage facility in a sedimentary reservoir. Boxes 1 to 4 represent the decrease of CO_2 partial pressure along fluid transfer pathways into a host reservoir. For our experiments, in box 1: P_{CO_2} = 100 bar (D1), box 2: P_{CO_2} = 60 bar (D2), box 3: P_{CO_2} = 25 bar (D3) and box 4: P_{CO_2} = 7 bar (P1).

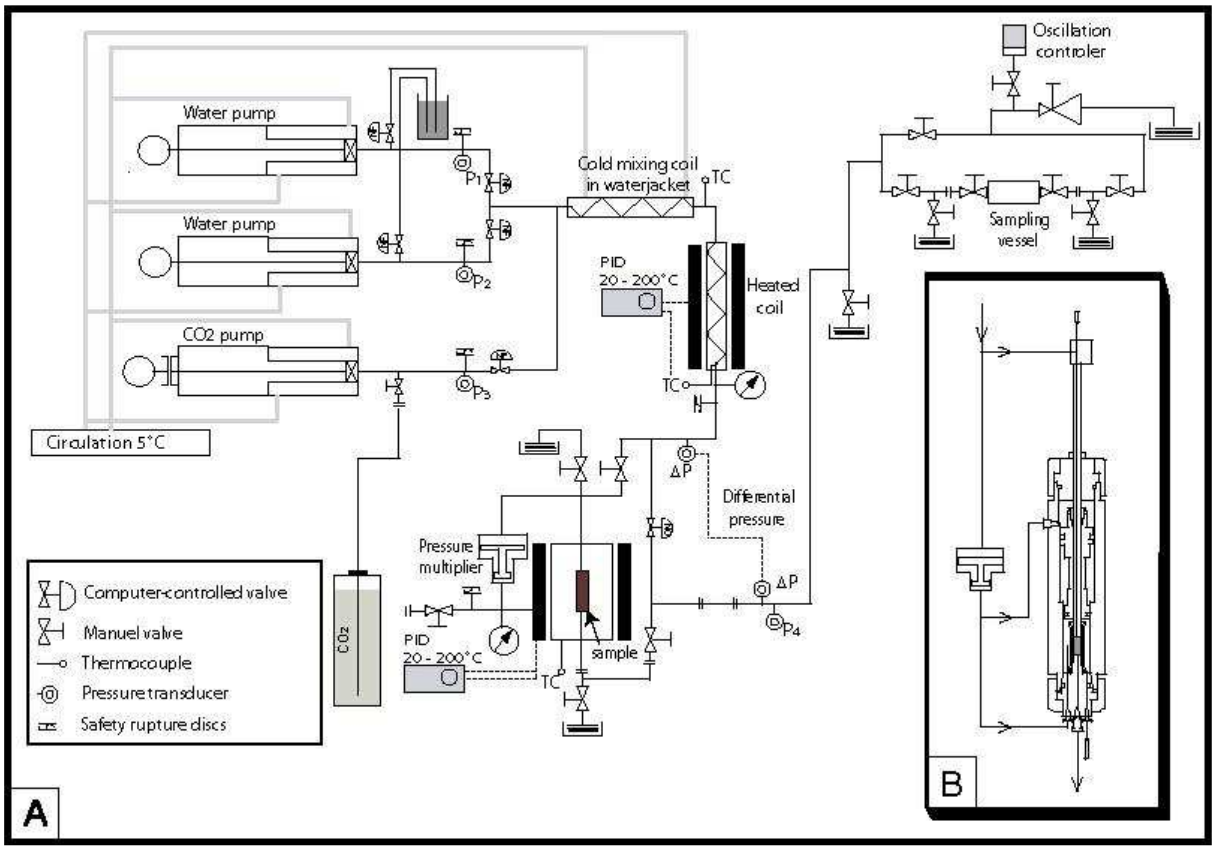

Fig. 2: Diagram of the experimental setup.

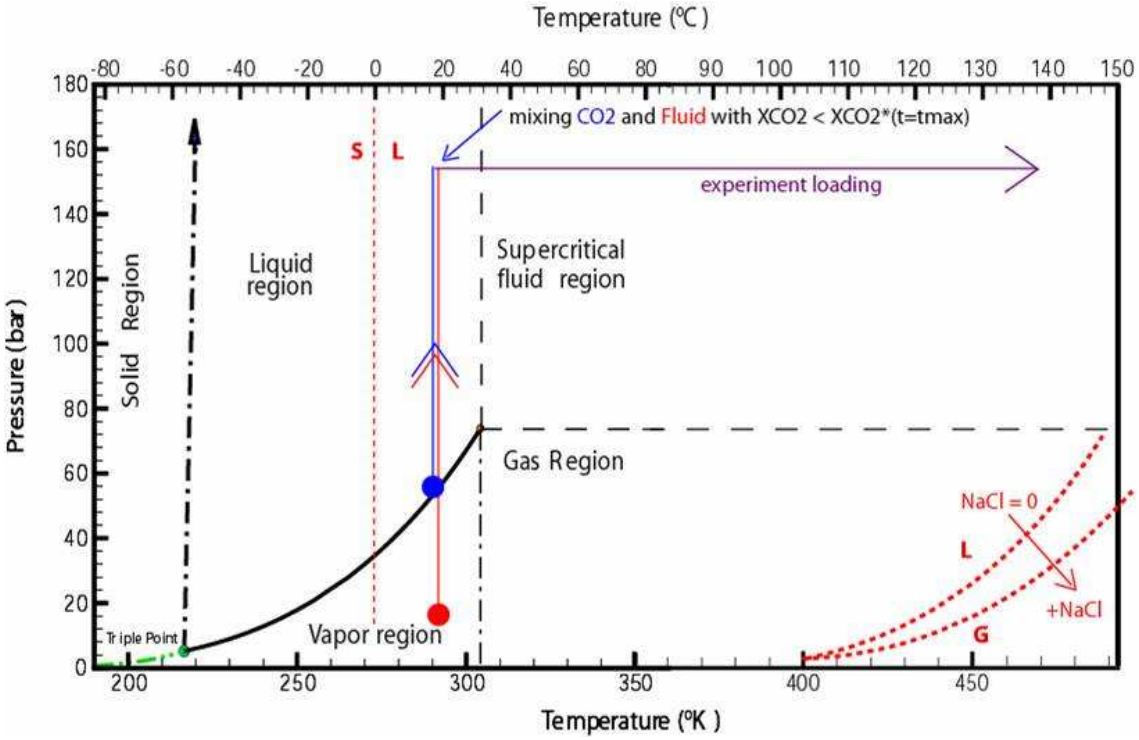

Fig. 3: *P* - *T* phase diagram for CO_2, with P-T path corresponding to CO_2-brine mixing.

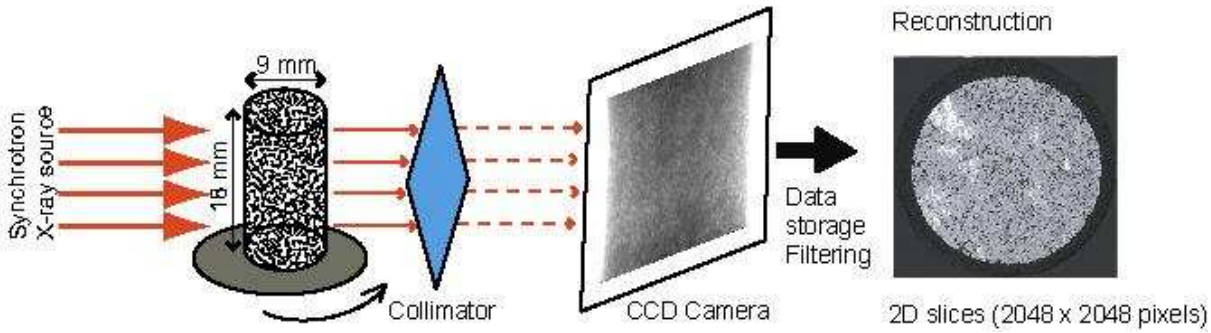

Fig. 4: Sketch diagram of the X-ray microtomography acquisition line.

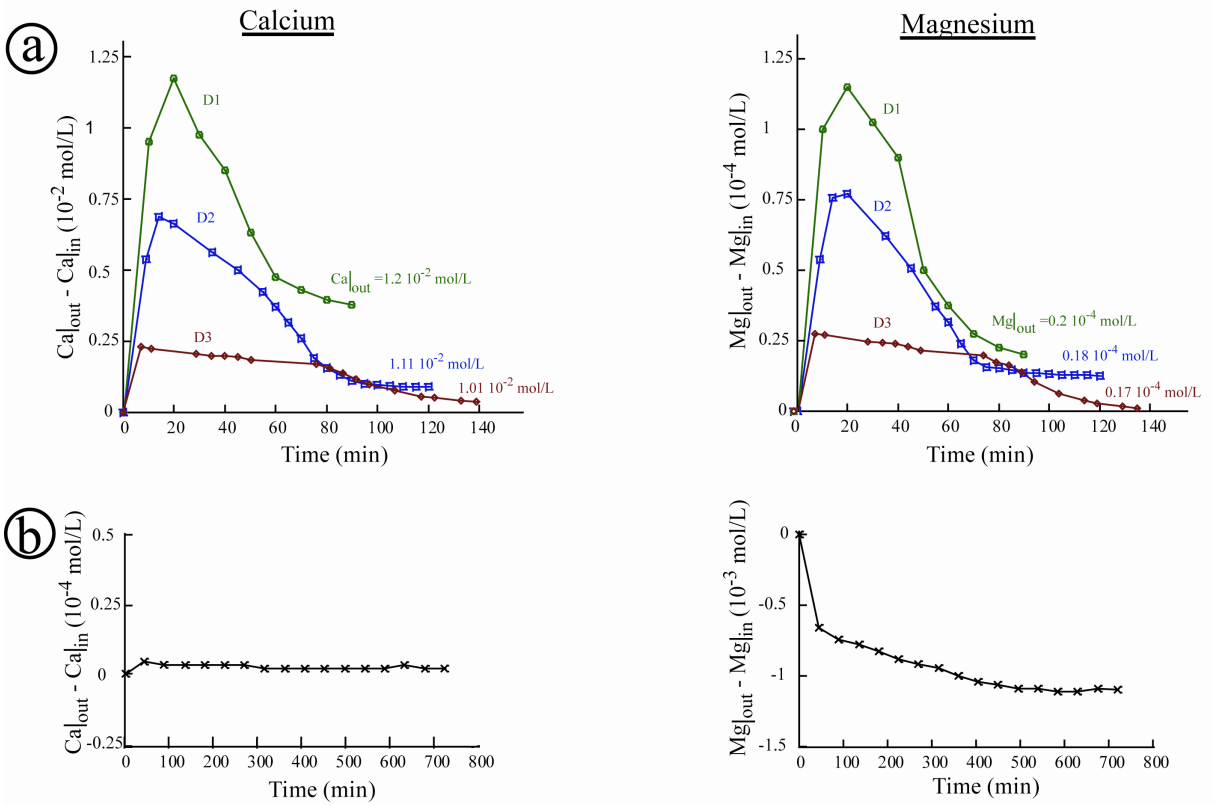

Fig. 5: Normalized time-resolved concentrations of *Ca* (on right) and *Mg* (on left). Results are presented for each experiment, D1 (circles), D2 (squares), D3 (diamonds) and P1 (crosses). Note that the time scale for the dissolution experiment is not the same as for the precipitation experiment.

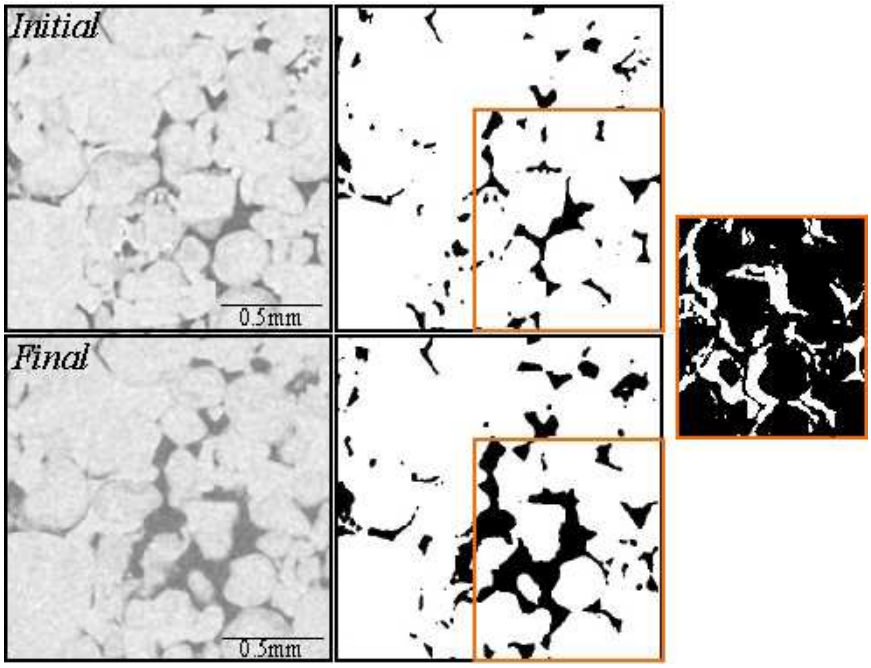

Fig 6: XMT cross-section of the sample used for experiment D1. Left column shows the X-ray images before and after the dissolution experiment. Grey levels indicate the X-ray absorption intensity. Middle column shows the corresponding binary images, with calcite indicated in white and voids in black. Dissolved calcite (in white) is visualized on the right hand figure.

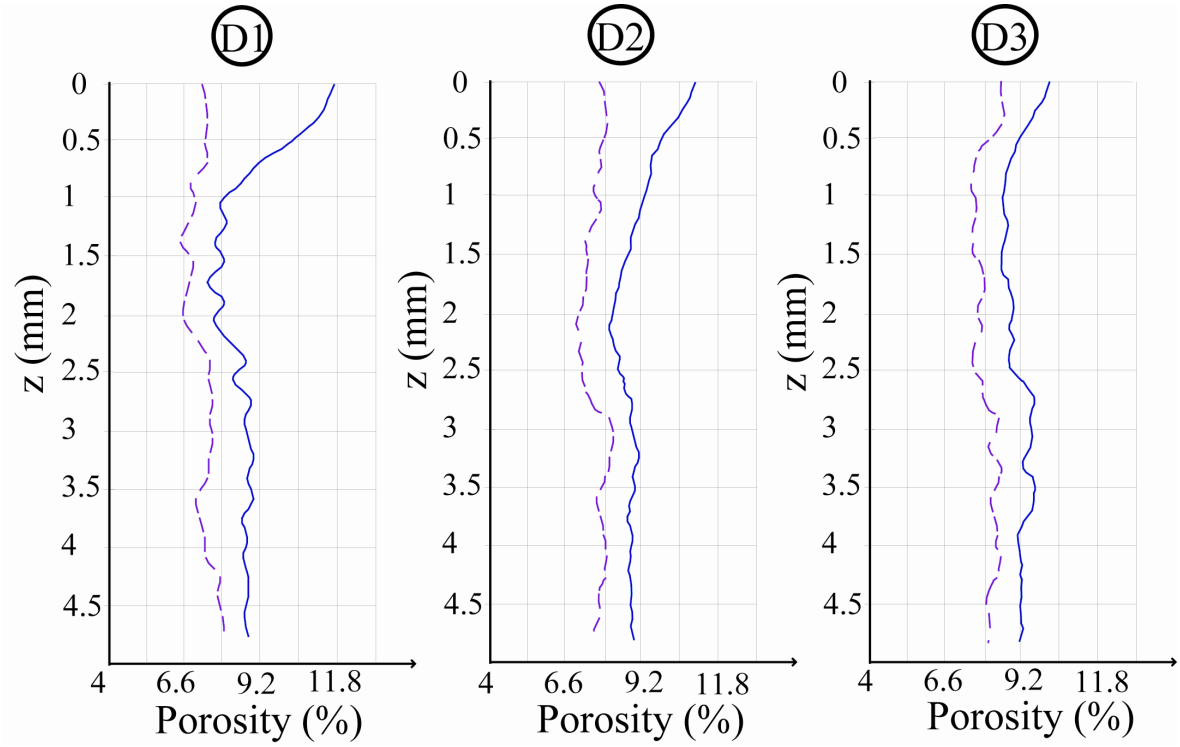

Fig. 7: *x-y* averaged porosity profiles along the samples in the flow direction (*z*) before the experiment (dotted) and after the experiment (plain).

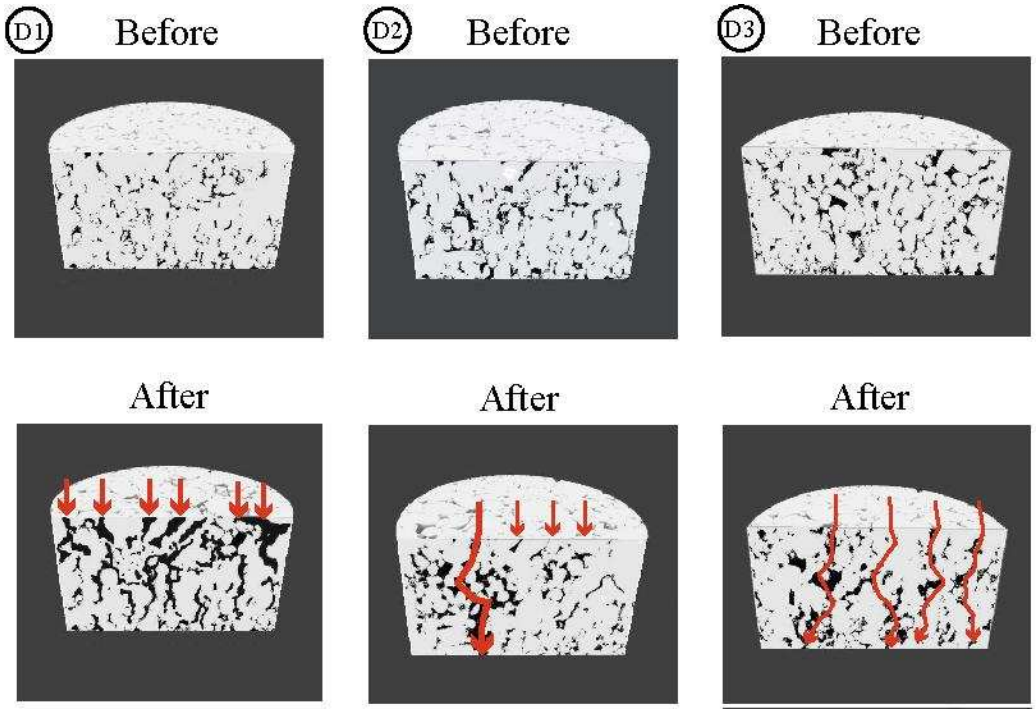

Fig. 8: 3D XMT images of the cores before (top line) and after (bottom line) for experiments D1, D2 and D3. Black and white areas represent voids and solids, respectively. Image dimensions are: diameter 9 mm and height 4.5 mm.

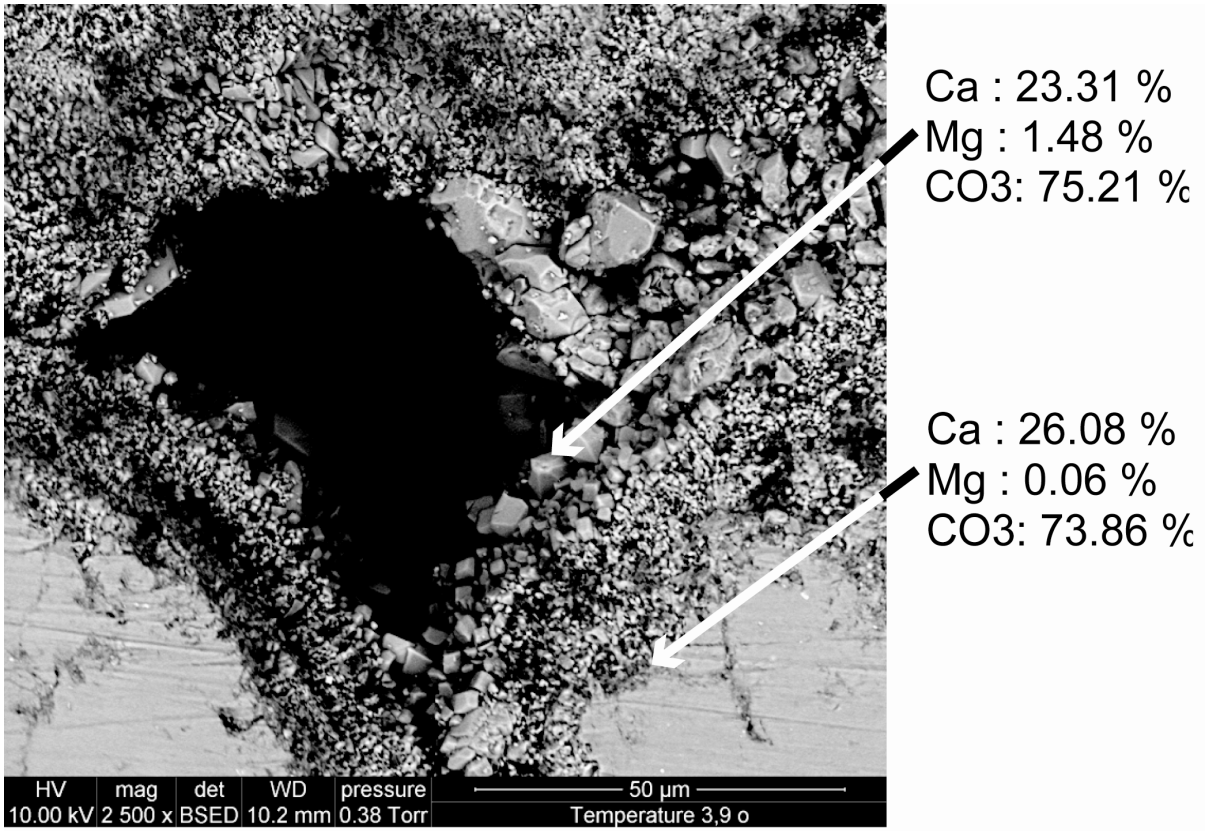

Fig. 9: Secondary electron micrographs (SEM) showing dolomite precipitated during experiment P1.

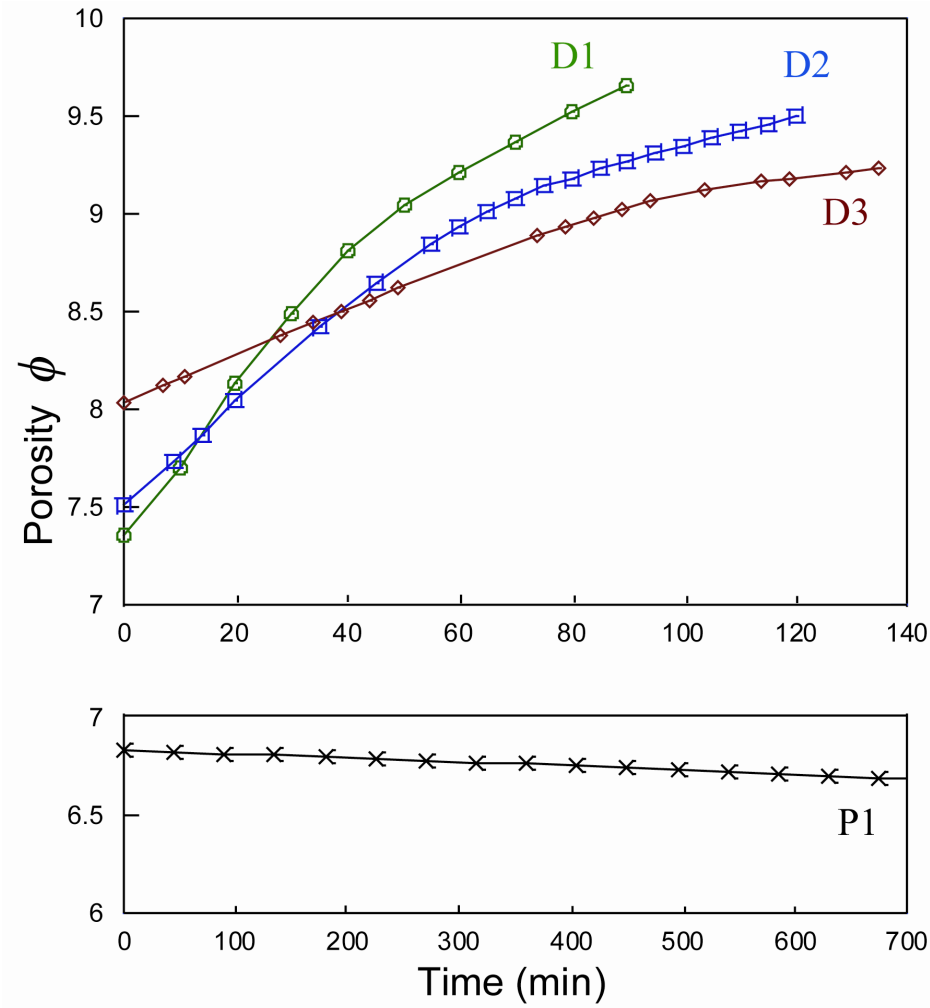

Fig. 10: Variation of porosity with elapsed time; D1 (circles), D2 (squares), D3 (diamonds) and P1 (crosses).

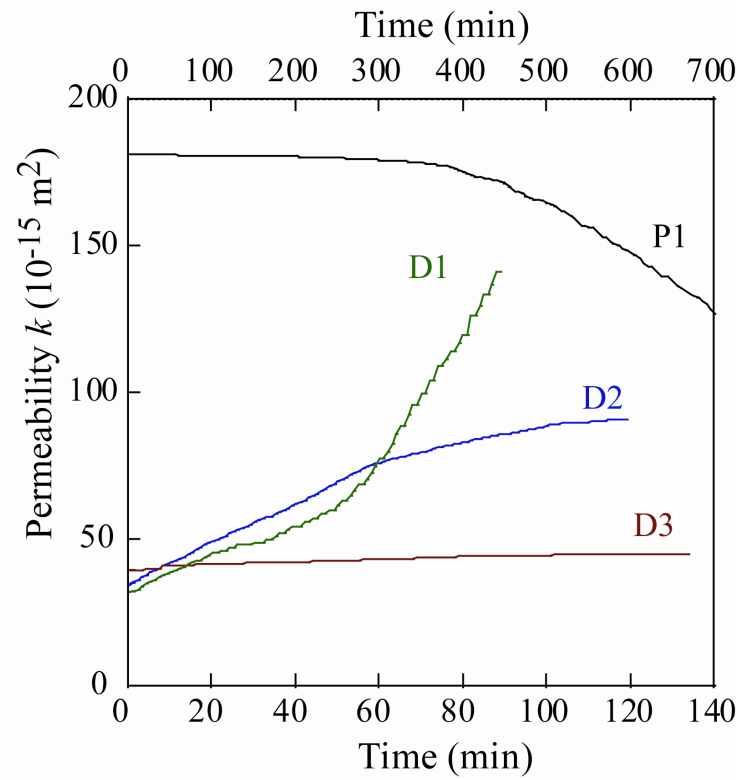

Fig. 11 : Variation of sample permeability with elapsed time for the dissolution experiments (D1 – D3) and the precipitation experiment P1.

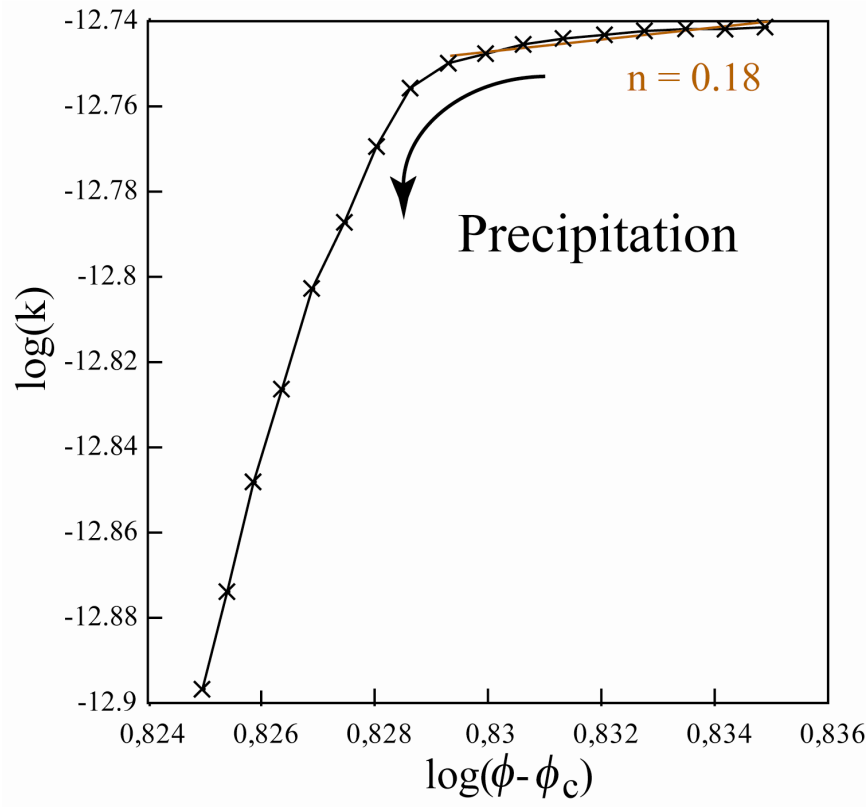

Fig. 12: Log permeability versus log porosity for the precipitation experiments.

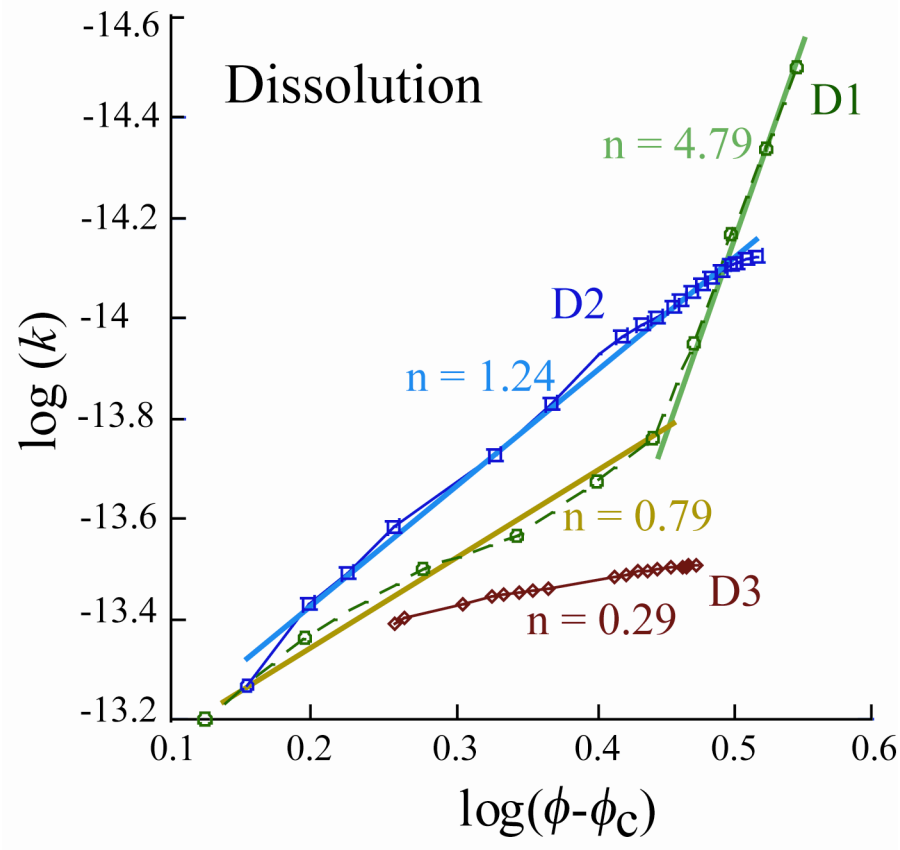

Fig. 13: Log permeability versus log porosity for the dissolution experiments D1 (circles), D2 (squares) and D3 (diamonds).

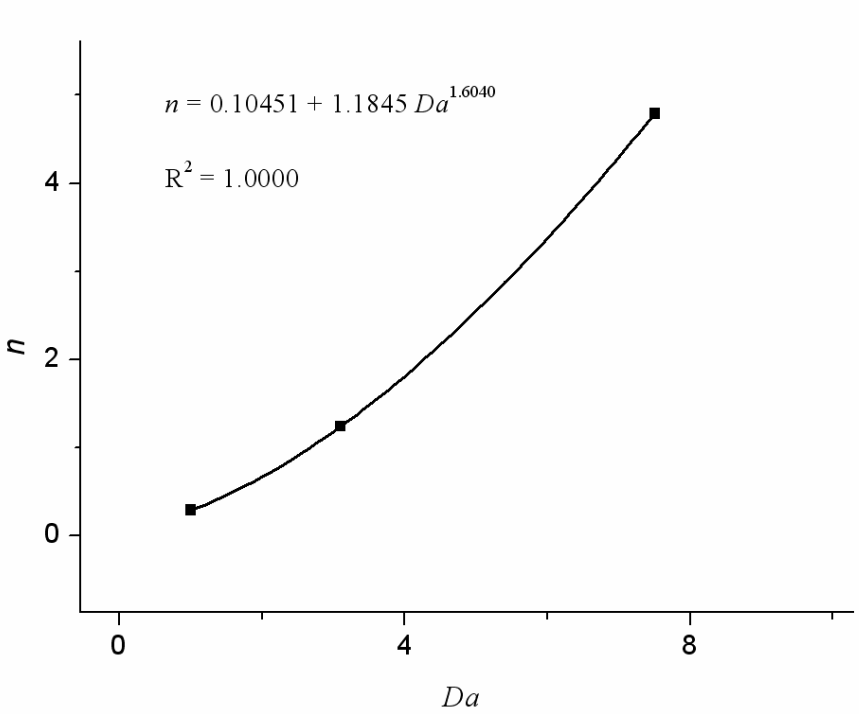

Fig. 14: Scaling exponent *n* versus value of the Damkolher number *Da* for the dissolution experiments D1 – D3. The regression coefficient *R* is optimal ($R^2 = 1$).